Atomically dispersed Fe atoms anchored on S and N–codoped carbon for efficient electrochemical denitrification

Jiacheng Li[a], Miao Li[a,1], Ning An[a], Shuo Zhang[a], Qinan Song[a], Yilin Yang[a], and Xiang Liu[a]

[a]School of Environment, Tsinghua University, Beijing 100084, China

Nitrate, a widespread contaminant in natural water, is a threat to ecological safety and human health. Although direct nitrate removal by electrochemical methods is efficient, the development of low-cost electrocatalysts with high reactivity remains challenging. Herein, bifunctional single-atom catalysts (SACs) were prepared with Cu or Fe active centers on an N-doped or S, N–codoped carbon basal plane for N_2 or NH_4^+ production. The maximum nitrate removal capacity was 7,822 mg N · g^{-1} Fe, which was the highest among previous studies. A high ammonia Faradic efficiency (78.4%) was achieved at a low potential (−0.57 versus reversible hydrogen electrode), and the nitrogen selectivity was 100% on S-modified Fe SACs. Theoretical and experimental investigations of the S-doping charge-transfer effect revealed that strong metal–support interactions were beneficial for anchoring single atoms and enhancing cyclability. S-doping altered the coordination environment of single-atom centers and created numerous defects with higher conductivity, which played a key role in improving the catalyst activity. Moreover, interactions between defects and single-atom sites improved the catalytic performance. Thus, these findings offer an avenue for high active SAC design.

single atom | nitrates | electrochemistry | catalyst

Water security is under threat by the various pollutants discharged from the growing array of human, industrial, and agricultural activities (1, 2). In particular, the ever-increasing utilization of nitrogen fertilizers and consumption of fossil fuels have resulted in severe nitrate pollution in surface water and underground aquifers, which disturbs the nitrogen cycle and threatens human health. The maximum nitrate concentration in drinking water should be 10 mg · L^{-1} N-NO$_3^-$, as stipulated by the World Health Organization and the US Environmental Protection Agency (3). The reduction of nitrates by electrochemical methods is a promising denitrification technology with the advantages of being clean, versatile, and convenient (4). Nitrate electroreduction (NIER) into value-added ammonia or environmentally friendly nitrogen gas uses electrons as a completely clean reactant, thus serving as a mild and facile approach to obtain chemical products and mitigate environmental concerns. Developing low-cost and highly efficient electrocatalysts for nitrate reduction during the treatment of polluted water is crucial for ammonia harvesting and water conservation.

Over the past few years, the nitrate removal performance of many different kinds of electrocatalysts, such as metals, metal oxides, alloys, polymers, and metal–molecular solid catalysts, has been evaluated (5–11). Among these, metal nanoparticles supported on carbon-based materials have attracted extensive attention owing to their high surface areas and metal utilization ratios. For example, corchorifolius-like carbon-microsphere–sealed Fe nanoparticles exhibited excellent N-removal capacity (1,816 mg · N · g^{-1} Fe) and high N$_2$ selectivity (98%). This unique structure with a high metal content is promising for electrodenitrification (5). However, as most studies have focused on metal active centers with nanometer dimensions, further atomic-level investigations are necessary. Previous study showed that the single Cu site in Cu-modified covalent triazine frameworks could efficiently promote the N−N bond

formation and N$_2$ production (10). In addition, Chen et al. reported a Cu–molecular (3,4,9,10-perylenetetracarboxylic dianhydride) solid catalyst for the electrochemical reduction of NO$_3^-$ into NH$_3$ with a maximum Faradaic efficiency of 85.9%. The superior catalytic activity was attributed to the unique 3d orbital (10) configuration of Cu on the molecular (11).

Over the last decade, single-atom catalysts (SACs) have attracted tremendous research interest and shown immense potential in practical applications because their metal atom utilization efficiencies are maximized, and the single-atom sites have unique electronic structures (12, 13). The rapid development of SACs in the field of electrochemistry (14) suggests that SACs with superior catalytic performance for NIER reactions could also be designed.

Generally, N-doped carbon materials with many defect sites are considered ideal supports for anchoring single transition–metal atoms. The use of such materials can also meet the demand for inexpensive SACs in large-scale electrochemical applications. N-doping can introduce extra defect sites in addition to intrinsic carbon defects, resulting in an asymmetric charge distribution (15). Consequently, more charge is transferred from metal atoms to neighboring N sites through the formation of strong chemical bonds. The strong metal–support interactions (SMSIs) caused by the defect sites contribute to the stabilization of single atoms and affect the intrinsic activity.

In this study, we prepared Cu- or Fe-doped carbon-based SACs with excellent catalytic performance for NIER. Over the

Significance

Denitrification by electrochemistry is a mild and efficient technique to reduce nitrate pollution in water. The urgency of finding a wastewater treatment has accelerated electrode material development. Here, (S) N-modified, carbon-supported Fe or Cu single-atom catalysts (SACs) were prepared using the anchoring effect of a defect-rich carbon basal plane with high activity and atom economy. Fe-CNS exhibits the highest Fe utilization in electrodenitrification among all reported studies. The coordination environment of Fe atoms was optimized by S-doping with asymmetric charge distribution and electron redistribution, resulting in higher activity of nitrate reduction. The atomic-level structure–activity relationship and reaction mechanism were investigated. The unique structure of Fe SACs renders them promising for the practical removal of pollutants in water.

ENVIRONMENTAL SCIENCES

www.manaraa.com

recent decades, electrochemical denitrification has been widely investigated, and different metallic electrode materials including Cu, Ag, Fe, Ti, and Au have been studied to further improve the catalytic performance (4, 5, 16–19). Among them, Cu and Fe are known to be the superior nonprecious metal catalysts for NIER because of their low prices, excellent electron-donating capabilities, and high activities (20, 21). Cu and Fe were chosen because their electrocatalytic activities are superior to those of other transitional metals (17, 20, 22). A postmodification method was used to further decorate the N-doped carbon material with S species. S-modification created more defects on the N-doped carbon basal plane, resulting in a more asymmetric charge distribution, which offered more opportunities to anchor metal atoms and regulate their coordination environments. (Soft) X-ray absorption spectroscopy (XAS) results verified the successful decoration of S species at the molecular level on both the N-doped carbon basal plane and the Fe active sites, which had a FeN_4S_2 coordination structure. The Fe SACs showed higher catalytic NIER activity than the Cu SACs, and the NIER Faradic efficiency was obviously improved upon S, N codoping. Based on the density functional theory (DFT) calculations, the enhanced NIER activity

of the Fe SACs was ascribed to lower free energy barriers for intermediates. The intrinsic electronic properties of the atomic coordination structure and the interactions between S/N defects and Fe single-atom sites were also investigated. This study not only developed highly active NIER SACs but also revealed the effects of S/N defects on catalysis and their SMSIs with metal atom centers at the molecular level.

Results

Characterization of SACs and Supports. As supports, an S, N–codoped carbon basal plane (CNS) and an N-doped carbon basal plane (CN) were prepared using thiourea, urea, and ammonium chloride as the S and N precursors, respectively, during the pyrolysis of pyromellitic dianhydride. To fabricate the corresponding SACs (e.g., Cu-CN or Fe-CNS), copper or ferric chloride was introduced during this process, as illustrated in Fig. 1A. The transmission electron microscopy (TEM) image (Fig. 1B) shows that the surface of CN is not smooth but exhibits many folds and defects, which could serve as anchoring sites for Cu or Fe single atoms with stable structures. As confirmed by the aberration-corrected high-angle annular dark-field scanning TEM (HAADF-STEM) images with
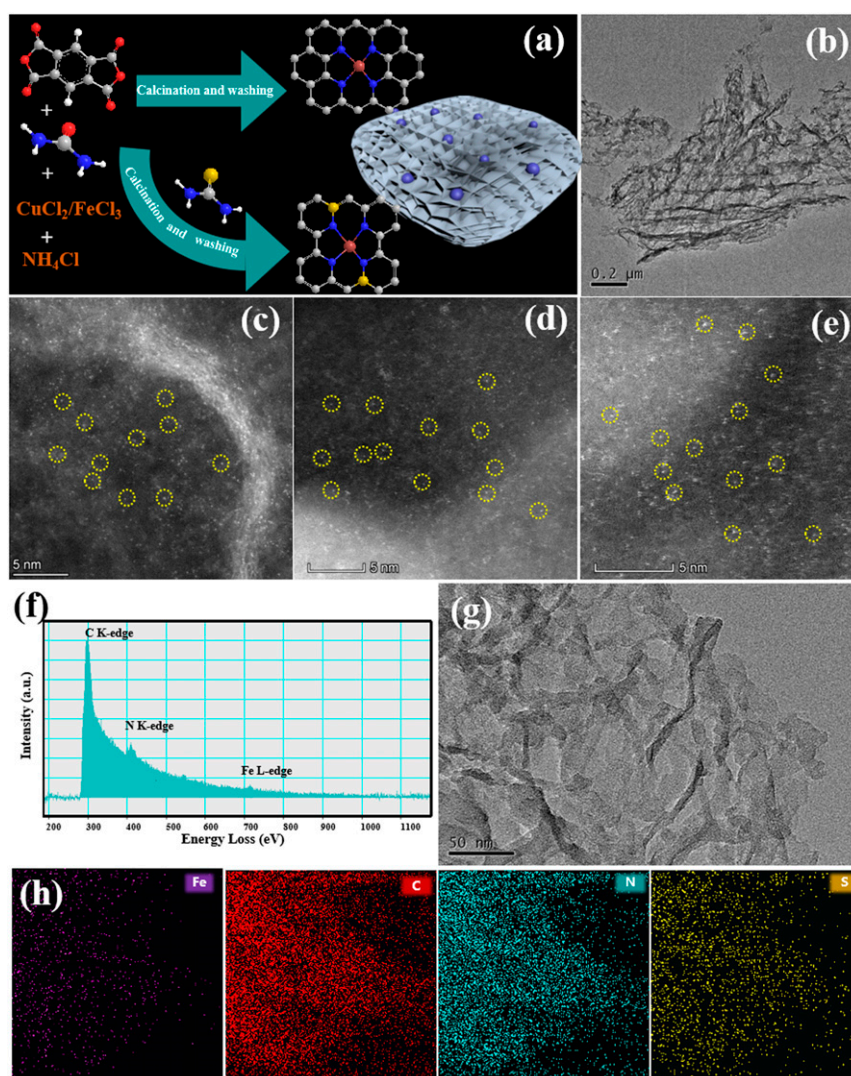

Fig. 1. Characterization of supports and SACs. (A) Schematic of the synthesis process for Cu/Fe-CN(S) SACs; (B) TEM image of CN framework; HAADF-STEM images of (C) Cu-CN SACs, (D) Fe-CN SACs, and (E) Fe-CNS SACs (the bright dots in yellow circles in (C), (D), and (E) represent Cu or Fe atoms); (F) electron energy loss spectroscopy spectrum of Fe-CN derived from the bright dot region in (D); (G) TEM image of Fe-CNS and corresponding X-ray energy-dispersive spectroscopy elemental mapping images of (H) Fe (purple), C (red), N (green), and S (yellow).

sub-Angström resolution, the as-prepared SACs have atomically dispersed Cu (Fig. 1C) or Fe (Fig. 1 D and E) atoms on the supports. The bright spots, as marked by yellow circles, were identified as single Cu or Fe atoms. The electron energy loss spectroscopy spectrum of Fe-CN derived from the bright region revealed C, N, and Fe signals, indicating Fe–N coordination (Fig. 1F). The TEM image of Fe-CNS (Fig. 1G) revealed no additional Fe clusters or particles on the surface of CNS on a large scale. Furthermore, the X-ray energy-dispersive spectroscopy elemental mapping images of Fe-CNS and Cu-CN (Fig. 1H and *SI Appendix*, Fig. S1) confirmed the successful introduction of N and/or S, and all the elements, including Fe or Cu, were distributed uniformly over the entire carbon basal plane. The metal contents of the Cu-CN, Fe-CN, and Fe-CNS SACs were 2.5, 2.1, and 2.0 weight (wt)%, as determined using inductively coupled plasma-optical emission spectrometry.

XAS is a well-established technique for investigating the chemical state and coordination environments of metal single-atom centers in SACs (23–25). The X-ray absorption near edge structure (XANES) spectra of Cu-CN, Fe-CN, and Fe-CNS at the Cu K-edge and Fe K-edge were collected to analyze their different coordination states. As shown in Fig. 2A, the rising edge of Cu-CN is located between those of CuO and Cu foil, indicating that the dominant valence state of the single Cu atom on CN is between Cu^0 and Cu^{2+}. The Fe K-edge XANES spectra of Fe-CN and Fe-CNS (Fig. 2C) display similar trends, and in both, the rising edge is located between those of Fe_2O_3 and Fe foil, similar to that for Cu-CN, clearly suggesting that the valence states of the Fe species are between Fe^0 and Fe^{2+}. A k^2-weighted Fourier-transform–extended X-ray absorption fine structure (FT-EXAFS) analysis was also conducted to probe the bonding structure between the heavy metal single atoms and the neighboring light elements in the Cu and Fe SACs. The EXAFS spectrum of Cu-CN (Fig. 2B) reveals one dominant peak centered at 1.5 Å, which results from the Cu–N scattering path. Furthermore, the absence of a characteristic Cu–Cu peak at 2.2 Å indicates the absence of Cu nanoparticles and the presence of atomically dispersed sites with a CuN_4 configuration on the carbon framework. For the Fe SACs (Fe-CN and Fe-CNS), the absence of an obvious peak at 2.2 Å, ascribed to Fe–Fe interactions in Fe foil, in the EXAFS spectra (Fig. 2D) confirms that no Fe nanoparticles were formed in these SACs. Instead, only a predominant peak at 1.5 Å, associated with the Fe–N scattering path, was observed for each Fe SAC. The XAS results confirm the high dispersion of single metal atom sites on CN(S), consistent with the aberration-corrected HAADF-STEM observations. Additionally, detailed information about the local coordination environment was achieved by quantitatively fitting the EXAFS data. The fitting parameters, including coordination numbers and atomic distances, are presented in *SI Appendix*, Table S1. The fitting results for Cu-CN and Fe-CN indicate that the Cu–N and Fe–N shells have distances of 1.82 and 1.92 Å, respectively, with coordination numbers of 4.3 and 4.1, respectively. These results are in agreement with the experimental data, and similar Cu–N and Fe–N parameters have been reported previously for Cu and Fe SACs (26–28). In contrast, the fitting results for Fe-CNS (Fig. 2D and *SI Appendix*, Table S1) revealed two kinds of bonds between the Fe atom and coordinated N atoms, with bond lengths of 1.98 and 1.87 Å. Thus, it is believed that S-doping affects the coordination between Fe and N atoms, influencing the length of the Fe–N bond in the FeN_4 configuration. After S-modification, a new highly dispersed metal center site with a FeN_4S_2 structure can form on CNS. It also should be noted that the EXAFS fitting can only give an average structural information of the metal center, other evidence for the existence of FeN_4S_2 coordination structure in Fe-CNS SACs is still needed. The structure is thermodynamically favored, as confirmed by previously reported DFT calculations (29). The binding energy of FeN_4S_2 structure (−10.56 eV) was much smaller than that of the FeN_3S_1 structure (−5.01 eV), which

suggested the S atoms were presumably bonded with the surrounding N or C atoms. Consequently, FeN_4 and FeN_4S_2 models were built based on experimental and theoretical studies (Fig. 2E).

The powder X-ray diffraction (XRD) patterns of the SACs (*SI Appendix*, Fig. S2) show no obvious peaks corresponding to Cu or Fe nanoparticles, which demonstrates the high dispersion of Cu/Fe species on CN(S). Furthermore, owing to its ability to identify Fe valence and coordination states, ^{57}Fe Mössbauer spectroscopy was performed to study the structure of the Fe species (30, 31). A single doublet appears in the spectrum of the Fe-CN sample (Fig. 2F). The absence of sextets and singlets indicates the absence of Fe–Fe bonds, which further confirms that the Fe species are atomically dispersed. Additionally, a wavelet-transform (WT)-EXAFS analysis was also conducted to supplement the FT-EXAFS analysis by providing resolution in both radial distance and k-space (32). In contrast to those of Fe foil and Fe_2O_3, the WT-EXAFS spectra of Fe-CN and Fe-CNS show only one peak with a maximum intensity at ~4.0 $Å^{-1}$ (Fig. 2F), which corresponds to Fe–N bonds. The WT-EXAFS spectrum of Cu-CN is similar, with only one peak attributed to Cu–N bonds (*SI Appendix*, Fig. S3). Taken together, these findings strongly indicate that both Cu and Fe are atomically dispersed on the (S)N-doped carbon matrix.

The elemental compositions and electronic states of the active sites, including the metal atom centers and their coordinated atoms, were further investigated using soft XANES and X-ray photoelectron spectroscopy (XPS). The XPS analysis, as a supplementary to the XAS analysis, can also reflect the bonding information of the metal centers and the surrounding heteroatoms (C,N or S).The C K-edge XANES spectrum of Fe-CNS (Fig. 3A) exhibits two peaks associated with C = C and C–C rings at 286.2 and 292.1 eV, respectively, whereas the peaks in the region of 287.4 to 288.6 are attributable to C–N–Fe(C) bonds (33, 34). The peaks in the N K-edge XANES spectrum (Fig. 3B) are ascribed to aromatic C–N–C bonds, graphitic N–3C bonds, and C–N σ bonds (33). The predominant peak in the S L-edge XANES spectrum (Fig. 3C) in the range 165 to 170 eV is attributed to C–S–C bonds (34). The XANES peaks are not smooth and have small split, which is different from normal N-doped carbon. This discrepancy is caused by the influence of the doped S atoms nearby (29). The successful introduction of S and N species into the carbon skeleton alters the uniform distributions of electrons in C–C or C = C bonds. As confirmed by the C 1s XPS spectrum (Fig. 3D and *SI Appendix*, Fig. S4 A and B), the deconvoluted peak at 286.0 eV corresponds to C–N bonds (35). The N 1s spectrum of Fe-CNS (Fig. 3) was deconvoluted into four types of N species at around 400.9, 400.3, 399.2, and 398.7 eV, which could be ascribed to graphitic N, pyrrolic N, Fe-Nx, and pyridinic N, respectively (36, 37). The N 1s spectrum of Fe-CN exhibited similar simulation results (*SI Appendix*, Fig. S4E). The ratios of the various N species are presented in *SI Appendix*, Table S2. Furthermore, as revealed by the N 1s XPS spectra of Fe-CN and Cu-CN (*SI Appendix*, Fig. S4 C and D), these samples and Fe-CNS show similar distributions of N species. In addition, the S 2p XPS results of CNS (*SI Appendix*, Fig. S4E) were analyzed in contrast to the S-states of Fe-CNS. The S $2P_{1/2}$ and S $2P_{3/2}$ peaks of CNS negatively shifted by 0.39 and 0.21 eV compared with those peaks in Fe-CNS. The deviation was caused by the electron-withdrawing effect between S and the surrounding Fe-N_4 sites (29). Therefore, the FeN_4S_2 structure dominates the active center site of Fe-CNS SACs. The C/N 1s XPS results are in accordance with the C/N K-edge XANES analysis. In addition, the Fe 2p XPS spectrum of Fe-CNS (Fig. 3F) shows two sets of peaks at 723.4 and 710.5 eV or 726.0 and 711.9 eV, corresponding to Fe(II) or Fe(III) species in the Fe $2p_{1/2}$ or Fe $2p_{3/2}$ region, respectively (38), which is consistent with the single Fe atom being positively charged. Similar results were obtained for the single Cu or Fe atoms supported on CN (*SI Appendix*, Fig. S5 A and B) [e.g., in the Cu 2p XPS
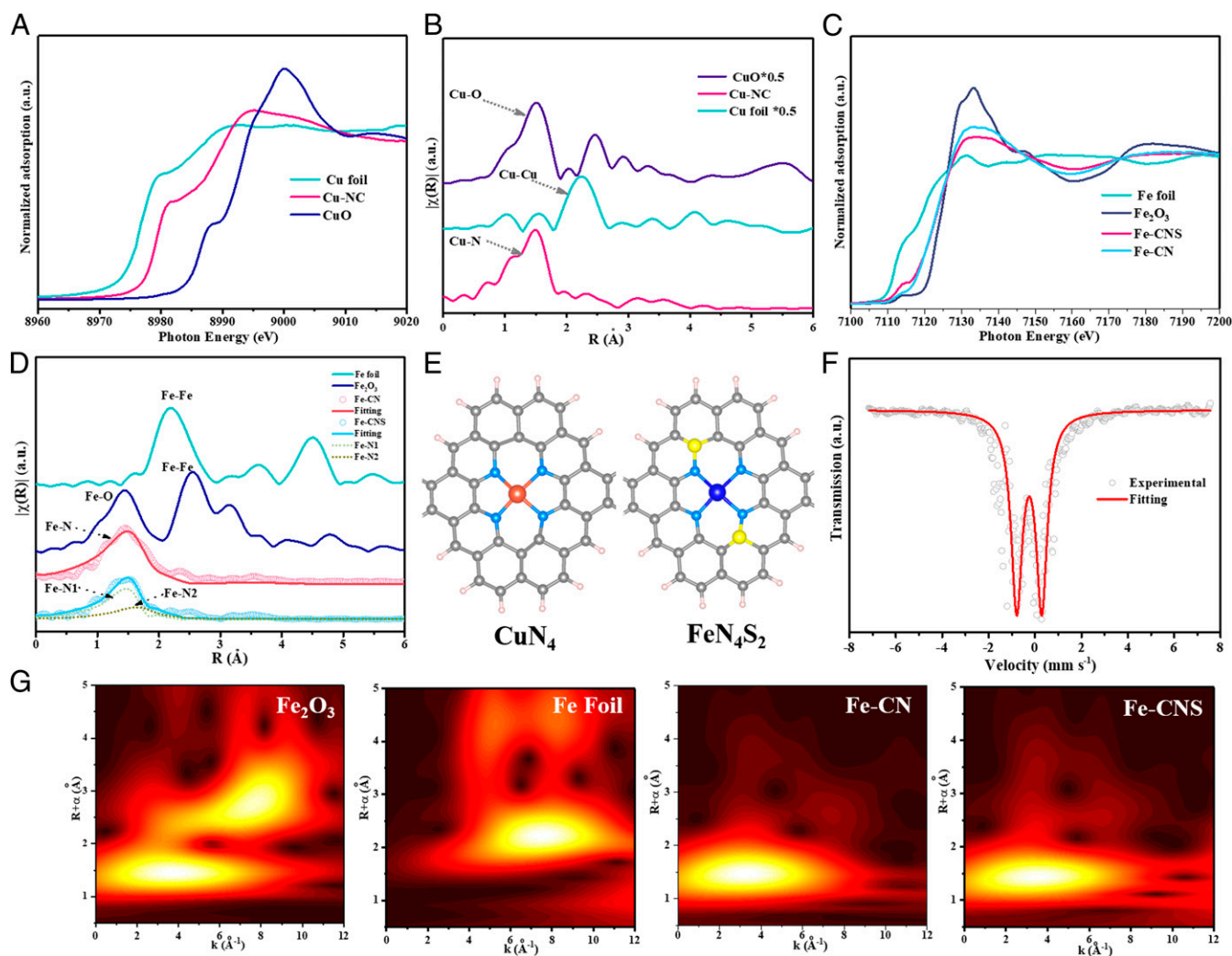
Li et al.
Atomically dispersed Fe atoms anchored on S and N–codoped carbon for efficient electrochemical denitrification

Fig. 2. Coordination environments of metal single-atom centers in SACs. (*A*) Normalized XANES spectra of Cu-CN, Cu foil, and CuO at the Cu K-edge and (*B*) corresponding k^2-weighted FT-EXAFS spectra. (*C*) Normalized XANES spectra of Fe-CN, Fe-CNS, Fe foil, and Fe$_2$O$_3$ at the Fe K-edge and (*D*) corresponding k^2-weighted FT-EXAFS spectra. (*E*) Fitted configurations of CuN$_4$ and FeN$_4$S$_2$ in Cu-CN and Fe-CNS. (*F*) ^{57}Fe Mössbauer spectra of Fe-CN SACs. (*G*) WT-EXAFS analysis of Fe$_2$O$_3$, Fe Foil, Fe-CN, and Fe-CNS.

spectrum of Cu-CN, the two peaks at 955.5 and 935.2 eV are ascribed to Cu(II) species, whereas those at 953.0 and 933.0 eV are assigned to Cu(I) species (39)]. Thus, based on the XANES and XPS results, the isolated single Fe or Cu atoms were positively charged owing to the electron-transfer effect of neighboring pyridinic N, resulting in SMSIs. The S 2p XPS spectrum of Fe-CNS (Fig. 3*G*) displays three peaks at 164.0, 165.4, and 168.3 eV, suggesting the formation of S–C, S-N and S–O bonds, respectively (40). Thus, S is doped in the CN skeleton, and its partial coordination with N or O should result in a positive charge. The successful anchoring of S was also verified by infrared (IR) spectral analysis (*SI Appendix*, Fig. S6*A*) and XPS survey of Fe-CNS (*SI Appendix*, Fig. S6*B*). The two obvious bands at 1,072 and 1,320 cm^{-1} correspond to C–S and C–N bonds, respectively (41). Thus, S-doping not only has an electron-transfer effect on the CN framework but also produces more defects. Both the XAS and XPS analysis of the Fe, C, N, and S elements were conducted to revel the coordination information of active center, and the FeN$_4$S$_2$ coordination structure was most likely existed in the Fe-CNS SACs.

The Raman spectra of CNS and CN both exhibit two obvious peaks at 1,362 and 1,569 cm^{-1}, ascribed to the D-band associated with carbon defects and the G-band associated with sp^2-hybridized C atoms (42). Generally, Raman method was widely used to characterize the defect sites in graphitic structure. Although it is hard to count the accurate number of defect sites, the intensity ratio of the D- and G-bands (I_D/I_G) could reflect the defect degree of carbon materials (43). The I_D/I_G value of CNS (1.09) was higher than that of CN (1.01), confirming the increased defect level after the S-doping in the CN framework. Furthermore, the overlap of the 2D and D- + G-bands at 2,500 to 3,000 cm^{-1} suggests a highly defective structure. The electronic structures of CNS and CN were further investigated using electron paramagnetic resonance (EPR) spectroscopy (Fig. 3*I*) at room temperature. The signal intensity increased to 1.6 times after S-doping, and the observation of a stronger spin intensity for CNS indicates that this support contains more defects than that of CN. The observation of a stronger spin intensity for CNS indicates that this support contains more vacancies than CN. The Raman and EPR results are in good agreement with the TEM images, suggesting a defect-rich structure for CNS. In addition, the UV (ultraviolet)-visible (UV-Vis) absorption spectra of CNS and CN (*SI Appendix*, Fig. S7) have absorption peaks in the visible–near-IR region, which are attributable to π–π stacking interactions (44). The higher peak intensity for CNS indicates that
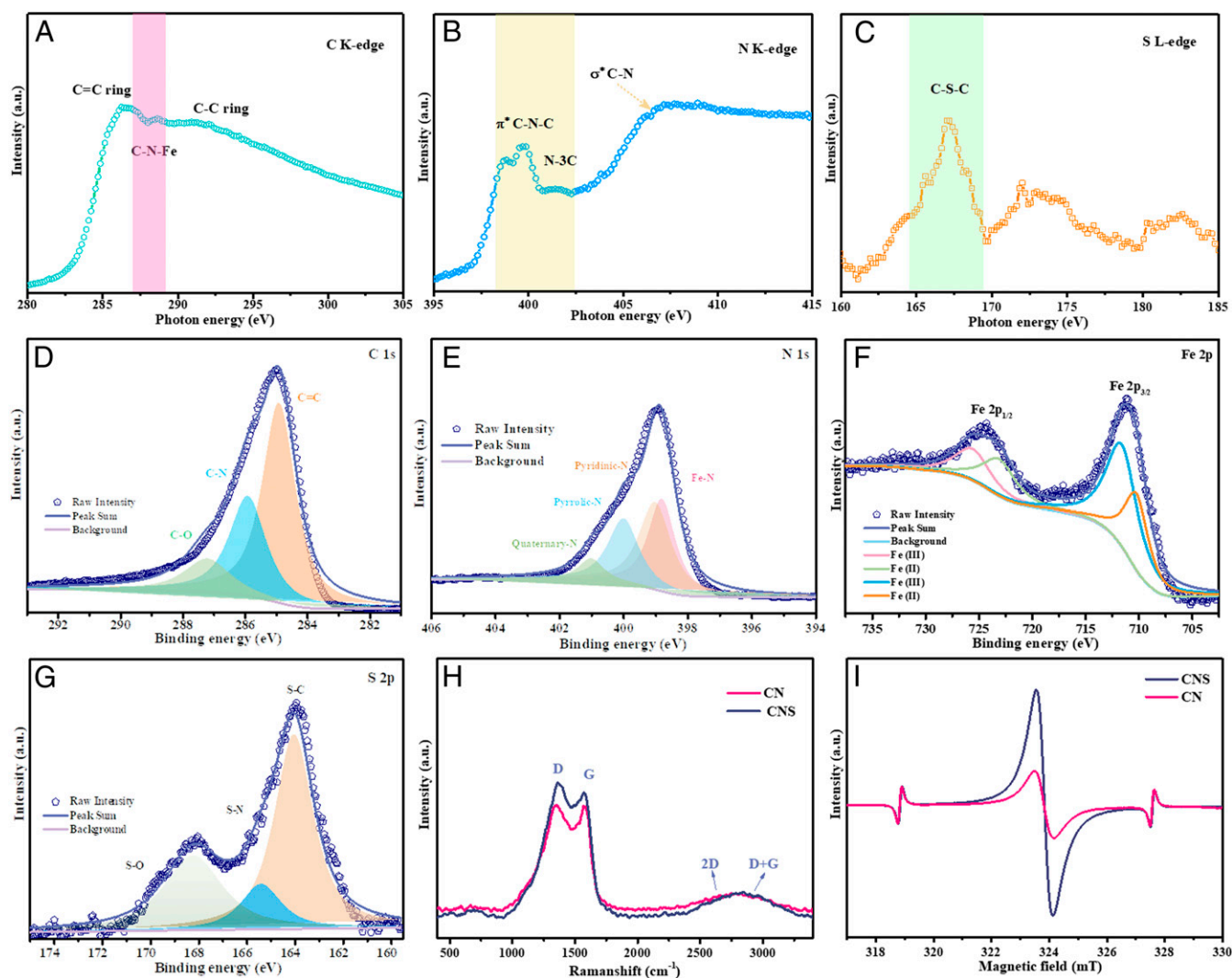
Li et al.
Atomically dispersed Fe atoms anchored on S and N–codoped carbon for efficient electrochemical...

Fig. 3. Elemental compositions and electronic states of active sites in SACs. (*A*) C K-edge, (*B*) N K-edge, and (*C*) S L-edge soft XANES spectra of Fe-CNS; deconvoluted high-resolution (*D*) C 1s, (*E*) N 1s, (*F*) Fe 2p, and (*G*) S 2p XPS spectra of Fe-CNS; (*H*) Raman spectra of CN and CNS; (*I*) EPR spectra of CN and CNS.

the amount of conjugated π-electrons increases after S-doping. The above results demonstrate that CNS is an excellent support with a defect-rich structure that not only offers numerous vacancies for anchoring single metal atoms but also lowers the charge-transfer resistance owing to the nonuniform distribution of electrons near the defects.

Evaluation of Catalytic Activity. The NIER profiles as a function of time at −0.67 V (versus reversible hydrogen electrode [RHE]) for all the SACs (Fig. 4*A*) are well fitted with the first-order kinetic model. The calculated reaction rate constant k for Fe-CNS ($2.3 \times 10^{-3} \cdot h^{-1}$) is larger than those for Cu-CN and Fe-CN ($1.5 \times 10^{-3} \cdot h^{-1}$ and $1.8 \times 10^{-3} \cdot h^{-1}$, respectively). This kinetic evaluation reveals that the Fe-CNS SAC has the best NIER catalytic performance. The pH of the solution slightly increased from 6.7 to 7.8 due to the production of ammonia and hydroxyl ion; the similar result was also reported by previous studies (7, 45). Since the SACs had similar metal contents, these results indicate that the NIER activity of the FeN$_4$ single-atom sites was better than that of the CuN$_4$ sites. The linear sweep voltammetry (LSV) curves in Fig. 4*B* indicate that Fe-CNS has the highest current density in the potential range from −0.6 to −0.8 V. The current density of Fe-CNS is -19.8 mA · cm^{-2} at a working

potential of −0.67 V, exceeding those of Fe-CN and Cu-CN. The electrochemical active surface areas (ECSAs) of the three SACs were also estimated from their double-layer capacitances, as shown in *SI Appendix*, Fig. S10 and Table S3. Fe-CNS has the largest ECSA, in accordance with its higher catalytic activity.

For Fe SACs with similar Brunauer–Emmett–Teller (BET) surface areas and Barrett–Joyner–Halenda (BJH) pore size distributions, S-doping obviously improved the electrocatalytic activity (*SI Appendix*, Fig. S8 and Table S3). The superior activity might be due to the introduced defect sites on CN or the unique FeN$_4$S$_2$ electronic structure. S-doping can create more disordered defect sites and shift the previously balanced electrons, thus providing CNS with good electrical conductivity. The numerous defects could also promote the catalytic activity. CNS and CN themselves show good catalytic NIER activities (*SI Appendix*, Fig. S9), and the rate constants for nitrate electrolysis on the CNS and CN are $1.6 \times 10^{-3} \cdot h^{-1}$ and $1.4 \times 10^{-3} \cdot h^{-1}$, respectively. Owing to the NIER activity of CNS, the N-removal capacity per unit mass of Fe in Fe-CNS was calculated by subtracting of nitrate removal capacity of CNS, which gave a value of 7,822 mg · N · g^{-1} Fe, which, to the best of our knowledge, was the highest value among prior results (*SI Appendix*, Table S4). The Fe SACs exhibits superior Fe utilization in electrodenitrification.
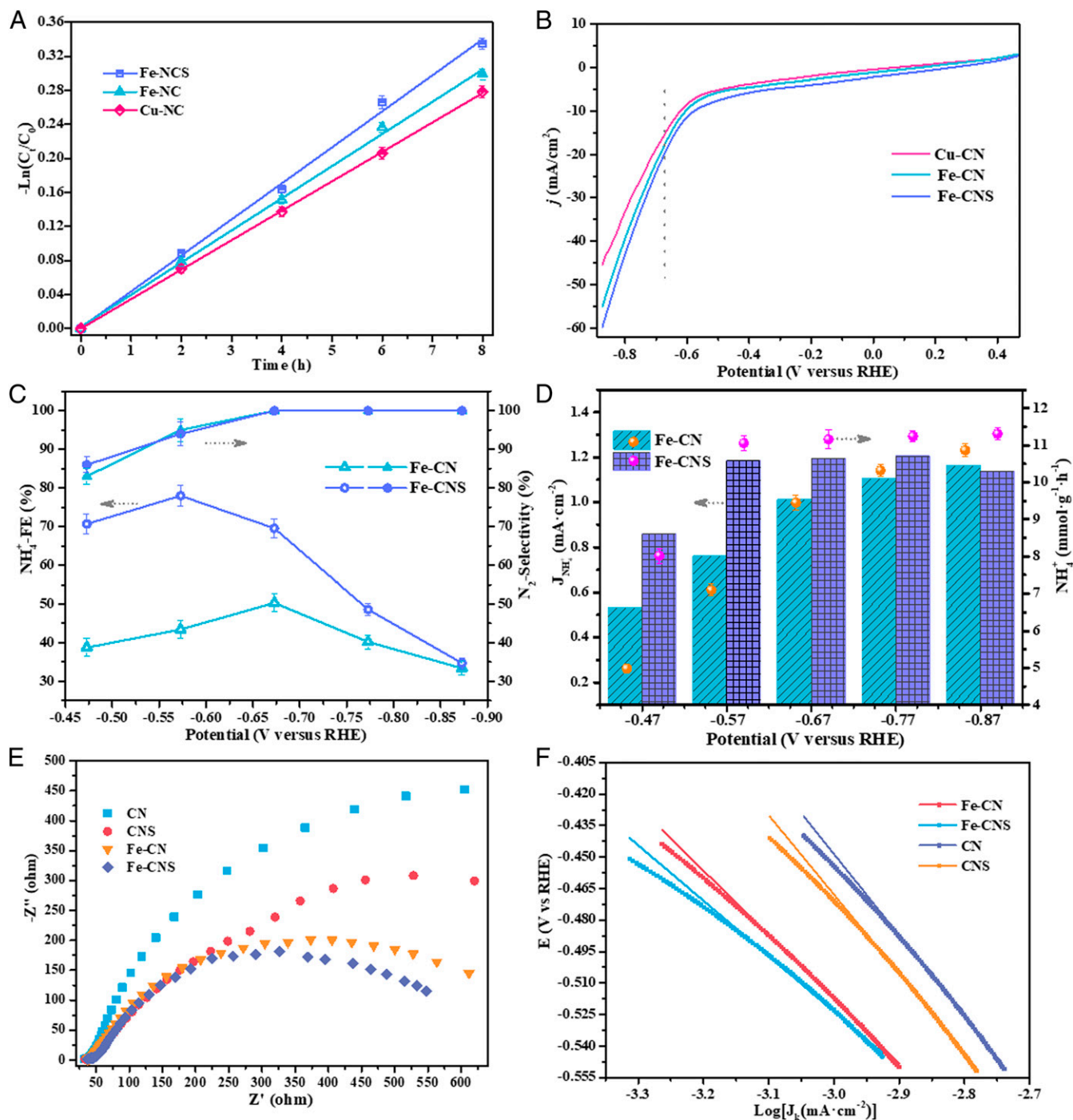
Fig. 4. Catalytic activity of SACs. (*A*) Kinetic linear fitting for nitrate removal over the SACs; (*B*) LSV curves for the SACs; (*C*) Faradaic efficiency for ammonia production in $NaNO_3–Na_2SO_4$ solution and N_2 selectivity in $NaNO_3–NaCl$ solution over Fe SACs at different potentials; (*D*) ammonia production and partial current densities; (*E*) electrochemical impedance spectra of Fe SACs, CN, and CNS; (*F*) Tafel slope analysis results of Fe SACs, CN, and CNS.

Because of their higher activities, further nitrate electrolysis was performed over the Fe SACs at various potentials (in the range from −0.47 to −0.87 V) and under different electrolyte conditions to reveal the ammonia Faradaic efficiency (NH_4^+-FE) at different potentials and the dependence of product selectivity on the electrolyte. For both Fe SACs, the variation in the NH_4^+-FE exhibits a typical volcano curve with decreasing potential (Fig. 4*A*). Compared with Fe-CN, Fe-CNS show higher NH_4^+-FE at all potentials. The potential required for achieving the

maximum NH_4^+-FE (78%) with Fe-CNS is −0.57 V, which is higher than that of Fe-CN (−0.67 V). As the potential becomes more negative, the hydrogen evolution reaction can complete with the NIER process, thus lowering the NH_4^+-FE. Here, harmless N_2 or valuable NH_4^+ were regarded as main products, and NO_2^- was the major by-product. Because of its instability, NO_2^- could be easily oxidized to NO_3^- by hypochlorite on anode and further participate in the reduction reaction. The N_2 selectivity of the Fe SACs was low at higher potentials but reached nearly 100% when

the potential was lower than −0.57 V. Thus, the Fe SACs show excellent potential for nitrate removal with double functions. In addition, control electrochemical experiments using Na$_2$SO$_4$ solution produced no ammonia (0 mmol · g^{-1} · h^{-1}), indicating that the source of ammonia is nitrate. The dependency of the partial current density and ammonia production on the applied potential was also investigated for the Fe SACs. As shown in Fig. 4D, Fe-CNS has a higher ammonia partial current density and produces more ammonia at most potentials. Moreover, decreasing the potential promotes ammonia production.

The enhanced catalytic performance of Fe-CNS was further confirmed by electrochemical impedance spectroscopy (EIS) (Fig. 4E and *SI Appendix*, Fig. S11A). The Nyquist plots of all samples show a partial circular arc in the high-frequency region, the radius of which reflects the value of the charge-transfer resistance (R$_{ct}$) (46). Compared with those of CN and Fe-CN, the Nyquist plots of CNS and Fe-CNS have shorter arc radii, which demonstrates that the S-doping can reduce the R$_{ct}$ and facilitate electron transfer.

In addition, Tafel plots were used to analyze the reaction kinetics of various catalysts (Fig. 4F and *SI Appendix*, Fig. S11B). The fitted Tafel slopes of Fe-CNS and CNS (264 and 378 mV · decade^{-1}, respectively) are smaller than those of Fe-CN and CN (306 and 388 mV · decade^{-1}, respectively). The lower Tafel slope for Fe-CNS suggests that the NIER process on this catalyst requires a lower overpotential and has faster reaction kinetics. Both the EIS results and Tafel plots confirm that the electronic structures are optimized by doping with S heteroatoms, which play a significant role in improving the catalytic performance by reducing the charge-transfer resistance and overpotential.

The reusability of Fe-CNS for NIER was evaluated. As shown in *SI Appendix*, Fig. S12, an inevitable loss in ammonia production occurs over five cycles. However, the metal active sites on Fe-CNS are stable, which facilitates its practical application. The stability of the SACs was also investigated using cyclic voltammetry (CV). In general, nitrates were reduced below the potential of −1.1 V (47). In our CV results (*SI Appendix*, Fig. S13), there was a weak broad peak in the range of −1.2 to −1.5 V, which was attributed to the nitrates reduction. The maximum peak current of Fe-CNS in this region was higher than that of Fe plate, which also confirmed a higher NIER activity of Fe-CNS SACs. The CV curves of Fe-CNS show almost no change after 100 cycles. In comparison, a Fe-plate electrode was seriously corroded by oxidation, with the CV curves showing apparent variations in current density (*SI Appendix*, Fig. S13 B–E). Thus, the Fe-CNS SAC shows both higher NIER activity and cycling stability. S-doping plays a significant role in improving the catalytic performance. Both the basal electrical conductivity and the activity of the metal atom centers in the SACs greatly influence the NIER process.

Theoretical Analysis. To further understand the structural properties of Fe-CNS and its reaction mechanism, a theoretical analysis was performed using DFT calculations. Owing to the various final products and intermediates, different reaction mechanisms have been reported for NIER (14, 48, 49). In particular, nitrate reduction to nitrite is the first step in the hydrogenation reaction (50). Furthermore, intermediate N atoms exist on the catalyst surface and influence the product selectivity (51).

The free energy was used to predict the direction of basic reaction based on the thermodynamic function. The change in the free energy for the NIER reaction was analyzed using different structural models. As depicted in Fig. 5A, nitrate first approaches and adsorbs onto the metal atom center. Then, one O atom is lost to form NO$_2$*. The changes in energy for this basic reaction on Cu-CN, Fe-CN, and Fe-CNS are 1.42, 2.02, and 2.37 eV, which are in accordance with the NIER activities of these catalysts. The experimental results showed that the Fe-CNS SACs have the best catalytic performance for nitrates removal,

and the NIER activity of Fe-CN is higher than that of Cu-CN. Subsequently, two O atoms are released from NO$_2$* to form the important N* intermediates. The N* intermediates couple with each other to form N$_2$ or are further hydrogenated to form NH$_3$ (Fig. 5B). The energy changes for the basic reactions from N* to N$_2$* and from N* to NH* on Fe-CNS are −0.14 and 2.78 eV, respectively, which indicates that the ammonia path is thermodynamically favored. Our experimental results indicate that the main product on different SACs for NIER is ammonia in the mixed solution of nitrates and sulfate. The DFT calculation results agree with the experimental ones, with the Fe-CNS catalyst showing the best catalytic performance for nitrate conversion to ammonia.

The introduction of S and N heteroatoms not only changed the metal centers but also produced numerous defects, thus promoting the catalytic performance. However, since the defect structure has not been accurately determined, we used the metal vacancies of FeN$_4$S$_2$ as model N-defects and investigated their effect on the NIER reaction. *SI Appendix*, Fig. S14 shows the differential charge density of Fe-CNS with and without N-defects. For the two structures, the charge density around the metal centers was poor, whereas charge accumulated on the neighboring N atoms. The electrons of the metal atoms were transferred to the adjacent N atoms, which is consistent with the XPS and XANES results. Moreover, the charge transfer of Fe atoms increased from 0.835 to 0.872 eV, when the interactions of the N-defects were considered, suggesting that the S-doped defects affect the electronic structure of the Fe atom. These results also suggest the presence of SMSIs, ensuring the high dispersion of metal atoms and their stable catalytic performance. Inspired by this finding, the relationship between the defects caused by S-doping and neighboring FeN$_4$S$_2$ sites was investigated using DFT calculations to reveal the effect of their interaction on the intrinsic NIER activity of Fe SACs (Fig. 5 C and D). A model combining N-defects and FeN$_4$S$_2$ sites was built and simulated, and the same basic NIER reactions were performed on the interacting Fe sites (Fe-N$_{def}$-int) and N-defects (N$_{def}$-Fe-int). The energy diagrams of the two sites show good potential for NIER with higher energy changes. This theoretical analysis revealed that the N-defects of the basal framework could catalyze the NIER process and also promote the catalytic performance of Fe single-atom sites due to electronic interactions.

Conclusions

In summary, electroconductive CN and CNS supports and the corresponding Cu or Fe SACs were prepared by a defect trapping strategy involving thermolysis. The HAADF-STEM images and XAS results confirmed the homogeneous distribution of single atoms. The kinetic rate constant of Fe SACs was found to be higher than that of Cu SACs, indicating that FeN$_4$ sites have higher intrinsic activity than CuN$_4$ sites for the NIER. Moreover, the maximum nitrate removal capacity was 7,822 mg · N · g^{-1} Fe, indicating the superiority of Fe SACs. S-doping of the support greatly influenced the catalytic activity, with Fe-CNS exhibiting a higher Faradic efficiency at a lower voltage (−0.57 V), as well as a lower charge-transfer resistance and overpotential. The coordination environment of the Fe atom and the conductivity of the carbon basal plane were obviously modified by S-doping. Both theoretical and experimental investigations indicated that the interaction between CNS and single Fe atoms is strong, which could optimize the electronic structure of the metal atom center and promote the catalytic performance for NIER. The Fe-CNS SAC also showed good cyclability, which facilitates its practical application. In addition to developing efficient SACs for NIER, this study provided insights into the influence of defects on SACs. This strategy can be used to design SACs and investigate their reaction mechanisms from the perspective of metal–support interactions.
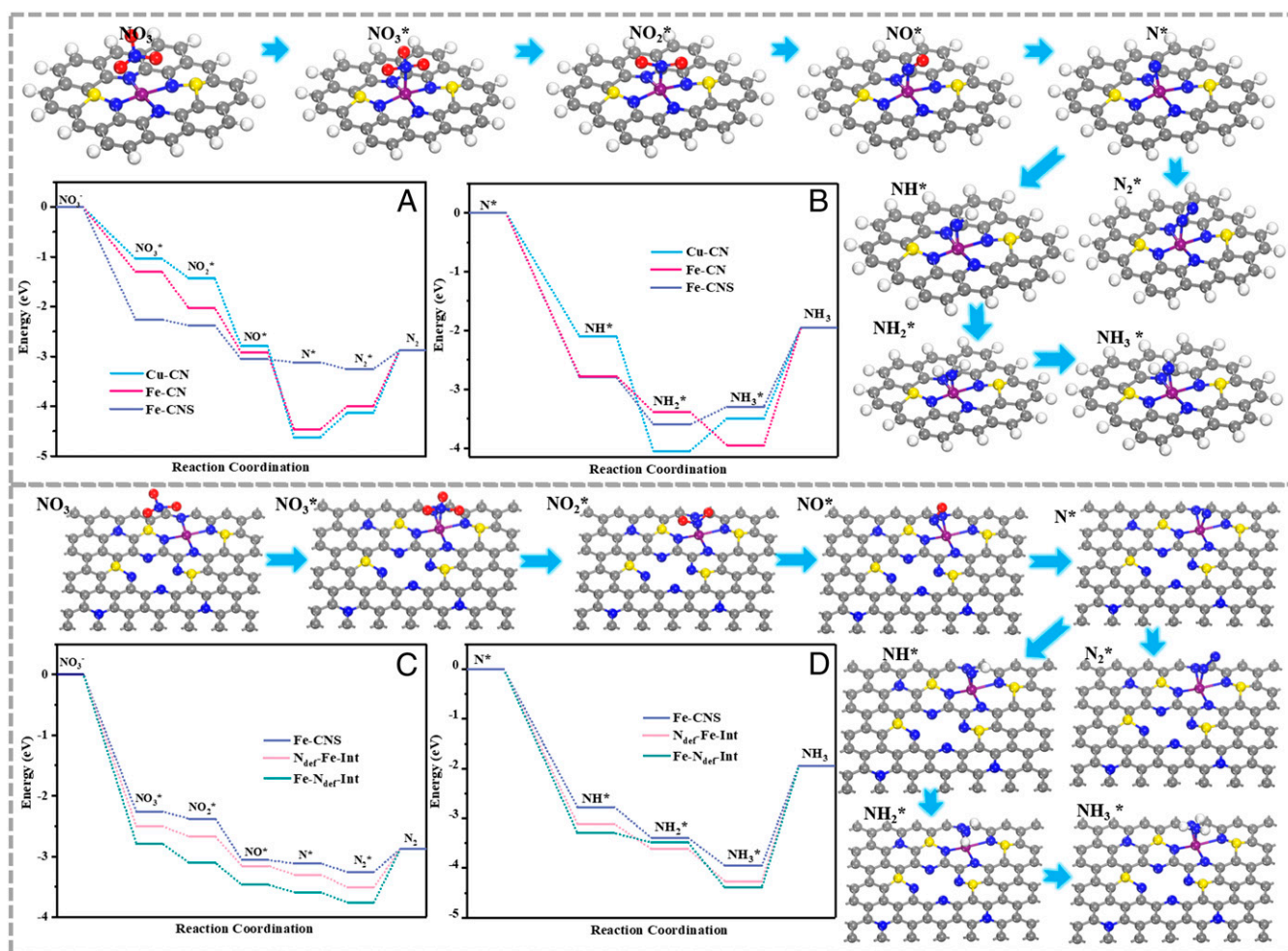
Li et al.
Atomically dispersed Fe atoms anchored on S and N–codoped carbon for efficient electrochemical denitrification

www.manaraa.com

Fig. 5. DFT calculations for the NIER process. (*A*) Energy changes during NIER for the path from nitrate to N₂ (NN) on the metal atom centers of various SACs; (*B*) energy changes for the path from intermediate N species to ammonia (NA) on various SACs; energy diagrams for the (*C*) NN path and (*D*) NA path on Fe atomic sites or N-defects considering their electronic interactions.

Materials and Methods

Synthesis of SACs. An N-doped and carbon base–supported single-atom metal catalyst (Cu-CN SAC) was prepared using a previously reported protocol but with slight modifications (52). Following the typical synthesis procedure for Cu-CN, a mixture of 2.1 g urea, 0.5 g ammonium chloride, 1.1 g pyromellitic dianhydride, and 0.19 g copper chloride dihydrate was ground in an agate mortar. The mixture was subsequently heated at 220 °C for 3 h in a muffle furnace and then washed with water, acetone, and ethanol before drying in a vacuum oven at 50 °C for 24 h. The primary product was then transferred to a tube furnace and calcined at 500 °C for 3 h at a ramp rate of 2 °C · min⁻¹ under an Ar atmosphere, affording the Cu-CN SACs. Finally, the obtained SACs were leached in a 0.5 M H₂SO₄ solution at 80 °C for 24 h to remove residual nanoparticles. Similarly, Fe-CN was also prepared by substituting the copper chloride dihydrate with an equal number of moles of ferric chloride in the above-mentioned process to fabricate Fe-CNS; the substitution was made with thiourea, which was added to the primary product in a mass ratio of 1:6, and the resulting mixture was ground in the agate mortar prior to calcination.

Synthesis of CN and CNS. N-doped and S, N–codoped carbon samples were prepared using a procedure similar to that for obtaining the corresponding SACs, without the addition of metal chlorides.

Characterization. TEM images were obtained using a JEM-2010 electron microscope (JEOL) operated at 100 kV. HAADF-STEM images were recorded using a Titan Cubed Themis G2 300 TEM apparatus (FEI) operated at 300 kV to investigate the distribution of single metal atoms at atomic resolution. The metal contents were determined by inductively coupled plasma-optical emission spectrometry on an iCAP 7000 analyzer. Wide-angle XRD patterns

in a 2θ range 5 to 90° were obtained using a D/max-IIIB diffractometer (RIGAKU) equipped with Cu-K-α1 radiation (λ = 1.5406 Å). The valences of the SACs were analyzed by XPS using an Escalab 250Xi photoelectron spectrometer (Thermo Fisher) with an Al-K-α radiation source (hυ = 1,486.6 eV). The C1's peak was used as a reference for the peak positions.

Nitrogen adsorption–desorption isotherms were collected using an Autosorb-1MP sorption analyzer (Quantachrome). The BET model was employed to calculate the specific surface area, and the BJH method was adopted to determine the pore size distribution from the adsorption branch. UV-vis absorption spectra were obtained using a UV2700 spectrophotometer (Shimadzu) in a wavelength range from 200 to 800 nm, with barium sulfate as the standard reflectance sample. Fourier-transform IR spectra were recorded for KBr pellets using a Nicolet iZ10 IR spectrometer (Thermo Fisher) in the 400 to 4,000 cm⁻¹ wavenumber range. Raman spectra were obtained using a LabRAM HR Evolution spectrometer (HORIBA) with a 532-nm He–Ne LASER. The acquisition time of each sample was 20 s, with three replications. EPR spectroscopy was performed using a JEOL FA-200 instrument at room temperature.

XANES and EXAFS spectroscopy of the Cu K-edge and Fe K-edge were recorded in fluorescence mode at room temperature using the 12-BM station at the Argonne National Laboratory (USA). Standard Cu and Fe foils were used to calibrate the energy, and CuO and Fe₂O₃ were employed as the reference samples, respectively. The soft XANES spectra of the C K-edge, N K-edge, and S L-edge were collected using the BL12B beamline at the National Synchrotron Radiation Laboratory (China).

The acquired EXAFS data were analyzed using the Athena and Artemis modules (implemented in the IFEFFIT software packages) to quantify the structural properties.
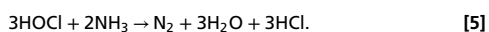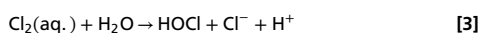
Electrochemical Measurements. The obtained SAC powders, acetylene black, and polyvinylidene fluoride were dispersed in a solution of N-methyl-2-pyrrolidone in a weight ratio of 8:1:1. The resulting solution was subsequently ultrasonicated to form a homogeneous ink. Thereafter, 140.6 μL ink was added dropwise on nickel foam of area 2.25 cm^2. The foam was vacuum dried and placed under 10 MPa of pressure to fabricate the electrode.

Electrochemical experiments were performed using a three-electrode cell system. Typically, a mixture of a nitrate solution (50 mL 100 mg/L N-NO$_3^-$) and 0.02 M Na$_2$SO$_4$ or NaCl was used for the electrode in the electroreduction process. A commercial Ru-Ir-TiO$_2$ electrode and a KCl-saturated Ag/AgCl electrode were employed as the anode and reference electrode, respectively. Before the measurements were obtained, the electrodes were treated at the working potential in the electrolyte to obtain a steady current–time curve. The potential versus RHE was calculated using the following equation:

$$E(\text{RHE}) = E(\text{Ag/AgCl}) + 0.22V + (0.059 \times \text{pH}). \qquad [1]$$

The NIER measurements were performed in a CHI-660E electrochemical workstation (CH Instruments) using the chronoamperometric (i–t) method. The concentrations of nitrates, nitrites, and ammonia in the solution were determined by colorimetry analysis based on UV spectrophotometry.

Nitrates can be gradually reduced to ammonia in NaNO$_3$-Na$_2$SO$_4$ solutions via the following route: NO$_3^*$→NO$_2^*$→NO*→N*→NH*→NH$_2^*$→NH$_3^*$. In a solution of NaNO$_3$ and NaCl, ammonia is oxidized to N$_2$ at the anode, in accordance with the following equations:

$$2Cl^- \rightarrow Cl_2(\text{aq.}) + 2e^- \qquad [2]$$

$$Cl_2(\text{aq.}) + H_2O \rightarrow HOCl + Cl^- + H^+ \qquad [3]$$

$$HOCl \rightarrow ClO^- + H^+ \qquad [4]$$

$$3HOCl + 2NH_3 \rightarrow N_2 + 3H_2O + 3HCl. \qquad [5]$$

The nitrate removal efficiency was estimated using the first-order kinetic model as follows:

$$C_t = C_0 \cdot \exp(-k \cdot t), \qquad [6]$$

where C_0 is the initial nitrate concentration, C_t is the nitrate concentration during electrolysis at time t, and k is the rate constant representing first-order kinetics.

The polarization curves of the samples were examined using LSV at room temperature at a scan rate of 50 mV/s.

The Faradaic efficiency for ammonia production (FE(NH$_4^+$)) and the corresponding partial current density of ammonia (J(NH$_4^+$)) were calculated using Faraday's law as follows:

$$FE(NH_4^+) = \left(n \times F \times C_{NH_4^+} \times V\right)/Q \qquad [7]$$

$$J(NH_4^+) = (Q \times FE(NH_4^+))/t, \qquad [8]$$

where F is the Faraday constant, n is the stoichiometric coefficient (for the conversion of NO$_3^-$ to NH$_4^+$), V is the volume of the nitrate solution, Q is the amount of electricity passing through the electrode, and t is the electrolysis time.

The Tafel equation (Eq. 9) was used to evaluate the relationship between the overpotential and current densities as follows:

$$\eta = a + b \cdot \log(j), \qquad [9]$$

where η is the applied overpotential, and j denotes the current density.

EIS analysis was conducted using an Ivium Electrochemical Workstation (Ivium) from 1,000 kHz to 0.01 Hz with an amplitude of 3 mV. Repeated CV experiments were performed at scan rates of 60 mV/s between 0.1 and −1.5 V (versus Ag/AgCl). The ECSA of the catalysts was obtained from the electrochemical double-layer capacitance (C_{dl}) in the non-Faradaic region with various potentials. Several CV curves were measured at various scan rates (2.5, 5.0, 7.5, 10.0, and 12.5 mV · s^{-1}) within a potential window from −0.45 to −0.65 V. C_{dl} was calculated using a linear fit of the capacitive current differences, $((J_A − J_B)/2)$, as a function of scan rates. ECSA was subsequently calculated using the ratio of C_{dl} and C_s, where C_s represents the general specific capacitance with an atomic smooth electrode under similar electrolyte conditions.

Computational Methods. Methods based on first principles (53, 54) were employed to perform all spin-polarized DFT calculations within the GGA using the Perdew–Burke–Ernzerhof (55) formulation. The Vienna Ab initio Simulation Package 5.4.1 software was used for DFT calculation. The projected augmented wave potentials (56, 57) were selected to describe the ionic cores, and the valence electrons were considered using a plane wave basis set with a kinetic energy cutoff of 400 eV. Partial occupancies of the Kohn–Sham orbitals were allowed using a Gaussian smearing method and a width of 0.05 eV. The electronic energy was considered to be self-consistent when the change in energy was smaller than 10^{-6} eV. The geometric optimization was considered to be convergent when the change in energy was smaller than 0.05 eV · Å^{-1}. The vacuum spacing in the direction perpendicular to the plane of the structure was 15 Å. The Brillouin zone integration was performed using 3 × 3 × 1 Monkhorst–Pack k-point sampling for the structure. Finally, the adsorption energies (E$_{ads}$) were calculated using E$_{ads}$ = E$_{ad/sub}$ − E$_{ad}$ − E$_{sub}$, where E$_{ad/sub}$, E$_{ad}$, and E$_{sub}$ are the total energies of the optimized adsorbate/substrate system, adsorbate in the structure, and clean substrate, respectively. The free energy was calculated using the following equation:

$$G = E + ZPE − TS, \qquad [10]$$

where G, E, ZPE, and TS represent the free energy, total energy obtained from DFT calculations, zero-point energy, and entropic contributions, respectively.

Data Availability. All study data are included in the article and *SI Appendix*.

1. Y. Tong *et al.*, Improvement in municipal wastewater treatment alters lake nitrogen to phosphorus ratios in populated regions. *Proc. Natl. Acad. Sci. U.S.A.* **117**, 11566–11572 (2020).

2. M. S. Mauter, P. S. Fiske, Desalination for a circular water economy. *Energy Environ. Sci.* **13**, 3180–3184 (2020).

3. A. S. Fajardo, P. Westerhoff, C. M. Sanchez-Sanchez, S. Garcia-Segura, Earth-abundant elements a sustainable solution for electrocatalytic reduction of nitrate. *Appl. Catal. B* **281**, 119465 (2021).

4. J. Martínez, A. Ortiz, I. Ortiz, State-of-the-art and perspectives of the catalytic and electrocatalytic reduction of aqueous nitrates. *Appl. Catal. B* **207**, 42–59 (2017).

5. L. Su *et al.*, Tailoring the assembly of iron nanoparticles in carbon microspheres toward high-performance electrocatalytic denitrification. *Nano Lett.* **19**, 5423–5430 (2019).

6. R. Jia *et al.*, Boosting selective nitrate electroreduction to ammonium by constructing oxygen vacancies in TiO$_2$. *ACS Catal.* **10**, 3533–3540 (2020).

7. J. Gao *et al.*, Non-precious Co$_3$O$_4$-TiO$_2$/Ti cathode based electrocatalytic nitrate reduction: Preparation, performance and mechanism. *Appl. Catal. B* **254**, 391–402 (2019).

8. C. Chen, K. Li, C. Li, T. Sun, J. Jia, Combination of Pd–Cu catalysis and electrolytic H$_2$ evolution for selective nitrate reduction using protonated polypyrrole as a cathode. *Environ. Sci. Technol.* **53**, 13868–13877 (2019).

9. E. Lacasa, P. Cañizares, J. Llanos, M. A. Rodrigo, Effect of the cathode material on the removal of nitrates by electrolysis in non-chloride media. *J. Hazard. Mater.* **213-214**, 478–484 (2012).

10. G.-F. Chen *et al.*, Electrochemical reduction of nitrate to ammonia via direct eight-electron transfer using a copper–molecular solid catalyst. *Nat. Energy* **5**, 605–613 (2020).

11. T. Yoshioka *et al.*, Electrocatalytic reduction of nitrate to nitrous oxide by a copper modified covalent triazine framework. *J. Phys. Chem. C* **120**, 15729–15734 (2016).

12. S. Ji *et al.*, Chemical synthesis of single atomic site catalysts. *Chem. Rev.* **120**, 11900–11955 (2020).

13. A. Wang, J. Li, T. Zhang, Heterogeneous single-atom catalysis. *Nat. Rev. Chem.* **2**, 65–81 (2018).

14. H. Zou, W. Rong, S. Wei, Y. Ji, L. Duan, Regulating kinetics and thermodynamics of electrochemical nitrogen reduction with metal single-atom catalysts in a pressurized electrolyser. *Proc. Natl. Acad. Sci. U.S.A.* **117**, 29462–29468 (2020).

15. H. Wang *et al.*, Doping monolayer graphene with single atom substitutions. *Nano Lett.* **12**, 141–144 (2012).

16. J. Virkutyte, V. Jegatheesan, Electro-Fenton, hydrogenotrophic and Fe^{2+} ions mediated TOC and nitrate removal from aquaculture system: Different experimental strategies. *Bioresour. Technol.* **100**, 2189–2197 (2009).

17. G. E. Dima, A. C. A. de Vooys, M. T. M. Koper, Electrocatalytic reduction of nitrate at low concentration on coinage and transition-metal electrodes in acid solutions. *J. Electroanal. Chem. (Lausanne)* **554–555**, 15–23 (2003).

18. M. Li, C. Feng, Z. Zhang, N. Sugiura, Efficient electrochemical reduction of nitrate to nitrogen using Ti/IrO$_2$-Pt anode and different cathodes. *Electrochim. Acta* **54**, 4600–4606 (2009).

ENVIRONMENTAL SCIENCES

Li et al.
Atomically dispersed Fe atoms anchored on S and N–codoped carbon for efficient electrochemical denitrification

www.manaraa.com

19. M. Li, C. Feng, Z. Zhang, S. Yang, N. Sugiura, Treatment of nitrate contaminated water using an electrochemical method. *Bioresour. Technol.* **101**, 6553–6557 (2010).

20. W. Teng *et al.*, Selective nitrate reduction to dinitrogen by electrocatalysis on nanoscale iron encapsulated in mesoporous carbon. *Environ. Sci. Technol.* **52**, 230–236 (2018).

21. D. Reyter, D. Bélanger, L. Roué, Nitrate removal by a paired electrolysis on copper and Ti/IrO$_2$ coupled electrodes - Influence of the anode/cathode surface area ratio. *Water Res.* **44**, 1918–1926 (2010).

22. J.-X. Liu, D. Richards, N. Singh, B. R. Goldsmith, Activity and selectivity trends in electrocatalytic nitrate reduction on transition metals. *ACS Catal.* **9**, 7052–7064 (2019).

23. C. Yan *et al.*, Coordinatively unsaturated nickel–nitrogen sites towards selective and high-rate CO$_2$ electroreduction. *Energy Environ. Sci.* **11**, 1204–1210 (2018).

24. M. Liu *et al.*, Atomically dispersed metal catalysts for the oxygen reduction reaction: Synthesis, characterization, reaction mechanisms and electrochemical energy applications. *Energy Environ. Sci.* **12**, 2890–2923 (2019).

25. Y.-S. Wei, M. Zhang, R. Zou, Q. Xu, Metal–organic framework-based catalysts with single metal sites. *Chem. Rev.* **120**, 12089–12174 (2020).

26. H.-Y. Gao *et al.*, Diamantane suspended single copper atoms. *J. Am. Chem. Soc.* **141**, 315–322 (2019).

27. L. Yuan *et al.*, Dynamic evolution of atomically dispersed Cu species for CO$_2$ photoreduction to solar fuels. *ACS Catal.* **9**, 4824–4833 (2019).

28. Q.-L. Zhu *et al.*, Atomically dispersed Fe/N-doped hierarchical carbon architectures derived from a metal–organic framework composite for extremely efficient electrocatalysis. *ACS Energy Lett.* **2**, 504–511 (2017).

29. Q. Li *et al.*, Fe isolated single atoms on S, N codoped carbon by copolymer pyrolysis strategy for highly efficient oxygen reduction reaction. *Adv. Mater.* **30**, e1800588 (2018).

30. Z. Zhang, J. Sun, F. Wang, L. Dai, Efficient oxygen reduction reaction (ORR) catalysts based on single iron atoms dispersed on a hierarchically structured porous carbon framework. *Angew. Chem. Int. Ed. Engl.* **57**, 9038–9043 (2018).

31. X. Long *et al.*, Graphitic phosphorus coordinated single Fe atoms for hydrogenative transformations. *Nat. Commun.* **11**, 4074 (2020).

32. J. Yang *et al.*, In situ thermal atomization to convert supported nickel nanoparticles into surface-bound nickel single-atom catalysts. *Angew. Chem. Int. Ed. Engl.* **57**, 14095–14100 (2018).

33. Y. Pan *et al.*, A bimetallic Zn/Fe polyphthalocyanine-derived single-atom Fe-N$_4$ catalytic site: A superior trifunctional catalyst for overall water splitting and Zn–air batteries. *Angew. Chem. Int. Ed. Engl.* **57**, 8614–8618 (2018).

34. P. Chen *et al.*, Atomically dispersed iron–nitrogen species as electrocatalysts for bifunctional oxygen evolution and reduction reactions. *Angew. Chem. Int. Ed. Engl.* **56**, 610–614 (2017).

35. S. Yang *et al.*, Exfoliated graphitic carbon nitride nanosheets as efficient catalysts for hydrogen evolution under visible light. *Adv. Mater.* **25**, 2452–2456 (2013).

36. G. Chen *et al.*, Zinc-mediated template synthesis of Fe-N-C electrocatalysts with densely accessible Fe-Nx active sites for efficient oxygen reduction. *Adv. Mater.* **32**, e1907399 (2020).

37. X.-B. Zhang *et al.*, Atomically dispersed hierarchically ordered porous Fe–N–C electrocatalyst for high performance electrocatalytic oxygen reduction in Zn-Air battery. *Nano Energy* **71**, 104547–104557 (2020).

38. J. Li *et al.*, Sub-nanocatalysis for efficient aqueous nitrate reduction: Effect of strong metal–support interaction. *ACS Appl. Mater. Interfaces* **11**, 33859–33867 (2019).

39. X. Xiao *et al.*, A promoted charge separation/transfer system from Cu single atoms and C$_3$N$_4$ layers for efficient photocatalysis. *Adv. Mater.* **32**, 2003082 (2020).

40. Y. Yang *et al.*, Z-scheme g-C$_3$N$_4$/C/S-g-C$_3$N$_4$ heterostructural nanotube with enhanced porous structure and visible light driven photocatalysis. *Micro. Meso. Mater.* **314**, 110891–110901 (2021).

41. A. Sakthivel, A. Chandrasekaran, S. Jayakumar, P. Manickam, S. Alwarappan, Sulphur doped graphitic carbon nitride as an efficient electrochemical platform for the detection of acetaminophen. *J. Electrochem. Soc.* **166**, B1461–B1469 (2019).

42. Y. He *et al.*, Single cobalt sites dispersed in hierarchically porous nanofiber networks for durable and high-power PGM-free cathodes in fuel cells. *Adv. Mater.* **32**, e2003577 (2020).

43. S. Li *et al.*, Incorporation of nickel single atoms into carbon paper as self-standing electrocatalyst for CO$_2$ reduction. *J. Mater. Chem. A Mater. Energy Sustain.* **9**, 1583–1592 (2021).

44. Y. Liu *et al.*, Highly enhanced visible-light photocatalytic hydrogen evolution on g-C$_3$N$_4$ decorated with vopc through π-π interaction. *Chin. J. Catal.* **40**, 168–176 (2019).

45. M. Kalaruban *et al.*, Enhanced removal of nitrate in an integrated electrochemical-adsorption system. *Separ. Purif. Tech.* **189**, 260–266 (2017).

46. H. Zhang *et al.*, Unveiling the activity origin of electrocatalytic oxygen evolution over isolated Ni atoms supported on a N-doped carbon matrix. *Adv. Mater.* **31**, e1904548 (2019).

47. G. E. Badea, Electrocatalytic reduction of nitrate on copper electrode in alkaline solution. *Electrochim. Acta* **5**, 996–1001 (2009).

48. Y. Yao, S. Zhu, H. Wang, H. Li, M. Shao, A spectroscopic study of electrochemical nitrogen and nitrate reduction on rhodium surfaces. *Angew. Chem. Int. Ed. Engl.* **59**, 10479–10483 (2020).

49. A. Verdaguer-Casadevall *et al.*, Probing the active surface sites for CO reduction on oxide-derived copper electrocatalysts. *J. Am. Chem. Soc.* **137**, 9808–9811 (2015).

50. G. E. Dima, G. L. Beltramo, M. T. M. Koper, Nitrate reduction on single-crystal platinum electrodes. *Electrochim. Acta* **50**, 4318–4326 (2005).

51. M. Duca, M. O. Cucarella, P. Rodriguez, M. T. M. Koper, Direct reduction of nitrite to N$_2$ on a Pt(100) electrode in alkaline media. *J. Am. Chem. Soc.* **132**, 18042–18044 (2010).

52. Y. Pan *et al.*, Regulating the coordination structure of single-atom Fe-N$_x$C$_y$ catalytic sites for benzene oxidation. *Nat. Commun.* **10**, 4290 (2019).

53. G. Kresse, J. Furthmüller, Efficiency of ab-initio total energy calculations for metals and semiconductors using a plane-wave basis set. *Comput. Mater. Sci.* **6**, 15–50 (1996).

54. G. Kresse, J. Furthmüller, Efficient iterative schemes for ab initio total-energy calculations using a plane-wave basis set. *Phys. Rev. B Condens. Matter* **54**, 11169–11186 (1996).

55. J. P. Perdew, K. Burke, M. Ernzerhof, Generalized gradient approximation made simple. *Phys. Rev. Lett.* **77**, 3865–3868 (1996).

56. G. Kresse, D. Joubert, From ultrasoft pseudopotentials to the projector augmented-wave method. *Phys. Rev. B Condens. Matter Mater. Phys.* **59**, 1758–1775 (1999).

57. P. E. Blöchl, Projector augmented-wave method. *Phys. Rev. B Condens. Matter* **50**, 17953–17979 (1994).

10 of 10 | PNAS
https://doi.org/10.1073/pnas.2105628118

Li et al.
Atomically dispersed Fe atoms anchored on S and N–codoped carbon for efficient electrochemical...